ADVANCED MATERIALS
www.advmat.de

Check for updates

Lipid-Bilayer-Supported 3D Printing of Human Cerebral Cortex Cells Reveals Developmental Interactions

Linna Zhou, Anne C. Wolfes, Yichen Li, Danny C. W. Chan, Ho Ko, Francis G. Szele, and Hagan Bayley**

Current understanding of human brain development is rudimentary due to suboptimal in vitro and animal models. In particular, how initial cell positions impact subsequent human cortical development is unclear because experimental spatial control of cortical cell arrangement is technically challenging. 3D cell printing provides a rapid customized approach for patterning. However, it has relied on materials that do not represent the extracellular matrix (ECM) of brain tissue. Therefore, in the present work, a lipid-bilayer-supported printing technique is developed to 3D print human cortical cells in the soft, biocompatible ECM, Matrigel. Printed human neural stem cells (hNSCs) show high viability, neural differentiation, and the formation of functional, stimulus-responsive neural networks. By using prepatterned arrangements of neurons and astrocytes, it is found that hNSC process outgrowth and migration into cell-free matrix and into astrocyte-containing matrix are similar in extent. However, astrocytes enhance the later developmental event of axon bundling. Both young and mature neurons migrate into compartments containing astrocytes; in contrast, astrocytes do not migrate into neuronal domains signifying nonreciprocal chemorepulsion. Therefore, precise prepatterning by 3D printing allows the construction of natural and unnatural patterns that yield important insights into human cerebral cortex development.

Human tissues consist of complex cellular patterns and structures that arise during development and are essential for tissue function.[1] Some of these self-organized patterns have been recapitulated in vitro, in 2D and 3D cell culture.[2,3] For example, human organoids derived from embryonic stem cells or induced pluripotent stem cells (iPSCs) are valuable tools for developmental biology, disease modeling, and regenerative medicine.[3,4] However, these structures generated from homogenous and uncontrolled cell aggregates spontaneously organize over time in an unpredictable and spatially disordered manner. Thus far, robust technologies have not existed that could control initial 3D cell patterns to study how this influences development and function. The ability to pre-position cell types in the initial state of the self-organization process could allow greater control over subsequent organized states. Geometric confinement with patterned surfaces for cell attachment at the onset of tissue self-organization can affect later-stage stem/progenitor cell self-organization events such as embryonic germ layer patterning[5] and neural rosette formation.[6] However, these approaches were conducted on 2D micro-fabricated surfaces and have not yet been extended to produce defined 3D geometries. Manually generated prepatterned 3D structures, e.g., assembled brain organoids[7] or functionally distinct cell clusters,[8] can be powerful tools for the study of neuronal migration across brain regions and brain region specification induced by signaling molecules. The mechanical automation of these spatial programming processes would increase the reproducibility and complexity of induced self-organization in 3D tissue models.

Human brain development is poorly understood due to lack of models and experimental tools. It is also one of the softest tissues and has remained a challenge for bioprinting. 3D bioprinting offers a fast prepatterning method but so far applications have been limited to the construction of tissues that are stiffer than the brain.[9,10] Efforts toward printing soft tissues have involved the addition of hard materials for mechanical support or have been limited to flat structures.[9,11,12] Neural stem cell (NSC) printing has relied on the incorporation of polysaccharides such as agarose, alginate and gellan gum,[13–16] or synthetic polymer-based scaffolds.[17,18] Additionally, the majority of the matrices and scaffolds used for bioprinting have

L. Zhou, A. C. Wolfes, H. Bayley
Department of Chemistry
University of Oxford
Oxford OX1 3TA, UK
E-mail: hagan.bayley@chem.ox.ac.uk
A. C. Wolfes, Y. Li, F. G. Szele
Department of Physiology, Anatomy and Genetics
University of Oxford
Oxford OX1 3PT, UK
E-mail: francis.szele@dpag.ox.ac.uk
D. C. W. Chan, H. Ko
Division of Neurology
Department of Medicine and Therapeutics
Li Ka Shing Institute of Health Sciences
Margaret K.L. Cheung Research Centre for Management of Parkinsonism
The Chinese University of Hong Kong
Hong Kong
The ORCID identification number(s) for the author(s) of this article can be found under https://doi.org/10.1002/adma.202002183.

© 2020 The Authors. Published by WILEY-VCH Verlag GmbH & Co. KGaA, Weinheim. This is an open access article under the terms of the Creative Commons Attribution-NonCommercial License, which permits use, distribution and reproduction in any medium, provided the original work is properly cited and is not used for commercial purposes.

DOI: 10.1002/adma.202002183

not recapitulated the functional properties and complexity of extracellular matrix (ECM). Other methods are yet to be tested for interrogating how initial cell positions trigger self-organization or recapitulate human brain developmental events.

We previously 3D printed tens of thousands of picoliter aqueous droplets conjoined by lipid bilayers to give 3D tissue-like materials.[19] Further, printed cellular structures were achieved by using agarose as matrix to give cartilage-like constructs.[20] To 3D print naturalistic and also artificially prepatterned brain tissues, we developed an enhanced droplet printing method that enables the construction of soft tissues with ECM and without hard materials to affect subsequent self-organization. Printed NSCs in ECM were viable, differentiated, and were functional. By spatially arranging NSCs inside Matrigel (basement-membrane like ECM), we triggered a series of cortical developmental events: neuronal migration, differentiation, axon outgrowth, and astrogenesis. Further, prepatterned astrocytes (surrounding NSCs) induced robust axonal fasciculation, suggesting that astrocytes participate in neural tract formation. By combining emerging fast cell programming methods[21,22] with our printing technique, we rapidly produced differentiated cortical tissues. Finally, we used spatial prepatterning to investigate cell migration in cortical tissues, which revealed that astrocytes preferentially maintained segregation from neurons indicating nonreciprocal chemorepulsion between neurons and astrocytes. We thereby demonstrate a 3D printing technique that provides predetermined cell patterning, enabling insights into subsequent self-organization processes that are important in cortical development such as axonal fasciculation and cell migration/segregation.

Reported droplet printing methods are limited to materials with low viscosities and low cell densities.[23] To improve the performance of our previously described droplet printer,[19] we designed a piezo driver capable of higher output voltages (Supplementary Information) to eject droplets containing materials with higher viscosity (Figure S1a, Supporting Information). The ejected, cell-laden, ECM-containing droplets spontaneously acquired a monolayer of lipids in the lipid-containing oil bath. Droplets positioned next to each other formed droplet interface bilayers (DIBs), which provided the crucial adhesive force for supporting the 3D architecture of the printed droplet networks and allowing patterning (**Figure 1**a).[24] Printing nozzles with different inner diameters were prepared and used to generate droplets with different sizes (Figure 1b). With the same nozzle, the ejected droplet size could be further tuned by adjusting the amplitude (voltage) and duration of the printing pulse. Using fluorescently labeled lipids, we also confirmed that DIBs were present between droplets (Figure 1c), enabling compartmentalization.[19,24] Thus, the droplets are separated from each other and do not exchange their ECM or cell contents during the printing process.

After printing, the structures were gelated by warming to room temperature (RT), during which the intact DIBs kept the droplet contents separated (Figure 1d, upper row). Matrigel gelation is slow at RT, whereas warming the printed droplets to 37 °C results in rapid rupture of the DIBs and droplet fusion (Figure 1d, middle row). Rupture of DIBs can also occur when the printing oil is exchanged with culture medium for postprinting culture. It is therefore essential to first gelate the ECM to maintain the 3D architecture of the network. To achieve this, we used a stepped temperature increase protocol. The printed network is first warmed to an intermediate temperature of ≈25 °C for 30 min, whereby partial gelation of Matrigel occurs, but where also the DIBs remain intact and maintain separation of droplet contents (Figure 1d, upper row). The network is subsequently incubated at 37 °C, whereupon the DIBs break and further gelation occurs across the former interface, leading to droplet connection without content mixing (Figure 1d, bottom row). The droplet network could then be transferred from the printing oil to culture medium without deformation or exchange of the cell contents between droplets (Figure 1e, Figure S1b, Supporting Information). The fluorescence of the labeled DIBs slowly disappeared from the networks within a few days while in culture (Figure S1c, Supporting Information), indicating that lipids had diffused away. Thus, ECM and cells were left behind without the need for any additional materials for mechanical support. Therefore, this technique allows the prepatterning of cells in scaffold-free soft ECM, avoiding the addition of biologically incompatible materials. The DIBs provide stabilization during the several hours required for materials such as Matrigel to gelate.

We next investigated whether we could construct soft human neural tissues using our printing technique. First, we performed 2D culture of human induced pluripotent stem cell (hiPSC)-derived NSCs in neural expansion medium with fibroblast growth factor (FGF2) and epidermal growth factor (EGF) for 4–7 d (**Figure 2**a). The hNSCs were then harvested and suspended in Matrigel at a cell density of 2×10^7 mL^{-1}. After printing with this "bioink," the constructed neural tissues (printed as $7 \times 7 \times 4$ droplet networks) were cultured in neural maintenance medium (NMM) for differentiation. At day 1 postprinting differentiation (ppd), the neural cells started to polarize, producing processes (Figure 2b). The neural cells projected processes across the former droplet boundaries into the adjacent droplets. The number of neural process outgrowths and branches increased over the first few days of culture (Figure S3a, Supporting Information) and more neural morphological changes appeared over longer differentiation times (Figure 2b, Figure S3b, Supporting Information). Notably, the printed cells exhibited high viability (≈96%), indicating that stress from the printing process had been limited (Figure 2c and Figure S2, Supporting Information). Immunostaining for the young neuron marker βIII-tubulin with TUJ1 antibodies revealed that neuronal processes extended over the first 2 weeks of differentiation (Figure 2d). The distribution of cells at day 14 ppd was heterogeneous, with TUJ1$^+$ neurons predominantly found at the surface of a construct whereas SOX2$^+$ neural progenitor cells were present throughout the whole construct (Figure S3c, Supporting Information).

We further studied the self-organization of neural cells in printed tissues by increasing the cell density to 3.5×10^7 mL^{-1}. Constructs printed at high cell density exhibited high viability and the cells were able to proliferate, resulting in dense structures (Figure 2e) by day 28 ppd. The high cell density also triggered SOX2$^+$ TUJ1$^+$ neural rosette formation at day 28 ppd (Figure 2e,f). Longer culture led to the formation of protuberances and an increasing number of deep cortical layer neurons (CTIP2$^+$, Figure 2g). Further, mature neurons (MAP2$^+$

© 2020 The Authors. Published by WILEY-VCH Verlag GmbH & Co. KGaA, Weinheim

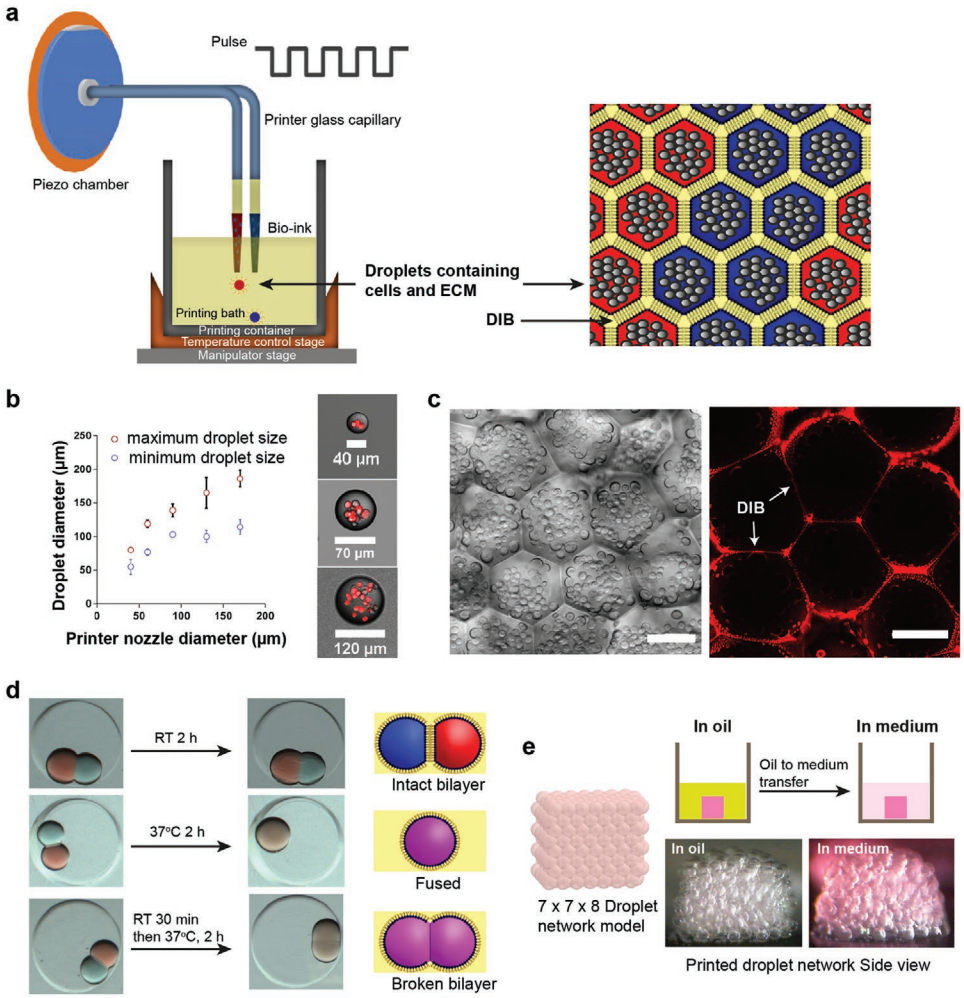


Figure 1. Lipid-bilayer-supported droplet bioprinting for soft tissues. a) Setup for printing water-in-oil droplets containing cells in ECM. The printer consists of a high-power piezo-driver for printing viscous materials, surface-modified glass printing nozzles, and a temperature-controlled manipulator stage. The manipulator stage moves under computer control and allows 3D positioning of droplets. Printed droplets are connected by adhesive DIBs to form patterned droplet networks. b) Ejected droplet sizes can be controlled by printer nozzle size. Droplet diameters were tuned by changing the voltage and width of the printing pulse ($n \geq 3$). Example images show droplets containing Matrigel and fluorescently labeled HepG2 cells. c) Left: bright-field image of part of a printed droplet network. Droplets contain Matrigel and HepG2 cells at 3×10^7 mL^{-1}. Right: Texas-red-labeled lipids reveal DIBs in a printed network. d) Matrigel droplet pairs containing dyes illustrate a stepped temperature increase approach to trigger DIB breakage and droplet connection. Top: DIB stays intact during a temperature increase from printing temperature (≈5 °C) to room temperature (RT) and is stable at RT for 2 h; middle: the DIB ruptures and the droplets fuse when the temperature is brought to 37 °C; bottom: the DIB breaks without droplet fusion after a stepwise temperature increase: from printing temperature to RT for 30 min, then RT to 37 °C for 2 h. e) Left, schematic of a $7 \times 7 \times 8$ droplet network (eight layers of 7×7 droplets). Top right: illustration of the transfer of a printed tissue from printing oil to culture medium. Bottom right: images of a printed $7 \times 7 \times 8$ droplet network (HepG2 cells (3×10^7 mL^{-1}) in Matrigel) in oil and then transferred to culture medium (side view). Scale bars are 100 µm, except the labeled scale bars in (b).

and NeuN$^+$) and astrocytes (GFAP$^+$) appeared after ≈2 months of differentiation (Figure 2h). Printed neural tissues were kept for over 100 d (Figure S4, Supporting Information). These data demonstrate the construction of viable neural tissues with different cell densities, and their self-organization and differentiation over long time periods.

Calcium ions (Ca^{2+}) are necessary in many cellular processes and serve as intracellular second messengers.[25] Spontaneous Ca^{2+} oscillations have been suggested to play a role in brain development.[26] Further, synchronized Ca^{2+} oscillations of interconnected neuronal networks are essential for brain functions.[27] To test the functionality of the neurons in our printed constructs, we performed Ca^{2+} imaging with Fluo-4. Time-lapse recordings revealed spontaneous Ca^{2+} oscillations in printed constructs after 4 d ppd (**Figure 3**a). Individual cell traces showed irregular patterns of calcium spikes (Figure 3b). Correlation coefficients were quantified and revealed low correlation between printed neural cells at an early differentiation stage (4 d ppd, Figure 3c). However, the cells exhibited more frequent and more regular Ca^{2+} oscillations at day 44 ppd (Figure 3d,e) and correlation coefficients revealed significantly

© 2020 The Authors. Published by WILEY-VCH Verlag GmbH & Co. KGaA, Weinheim

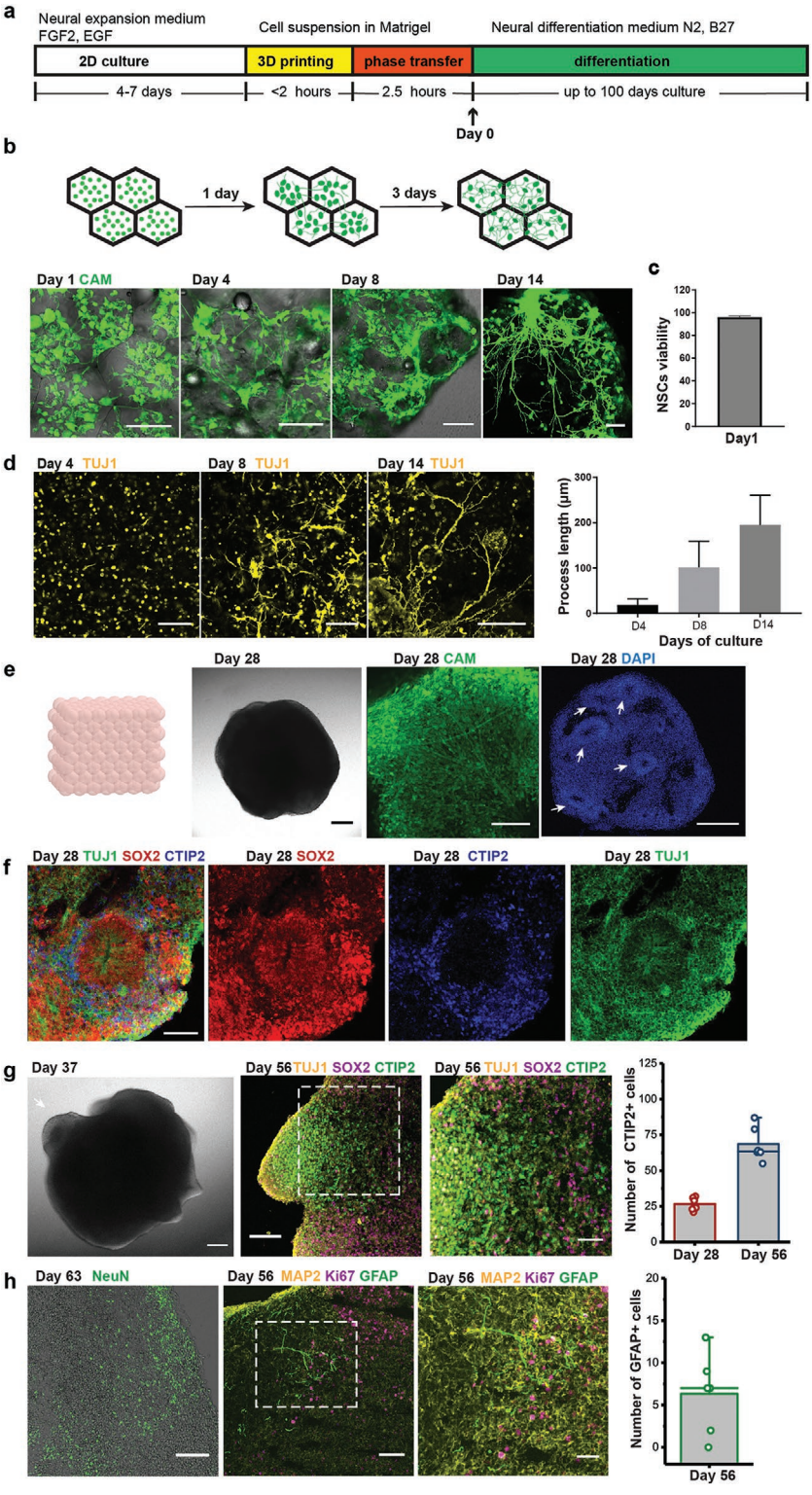


Figure 2. Printed neural tissues recapitulate cortical development events. a) Timeline for the production of 3D neural tissues. Further details are described in the Experimental section. FGF2, fibroblast growth factor; EGF, epidermal growth factor. b) Process formation in printed droplets during postprinting differentiation (ppd). Live cells were stained with Calcein AM (CAM). Example images of 1, 4, 8, and 14 d ppd show that printed NSCs project processes across droplets and form more polarized morphology over time. c) 96 ± 1% cell viability at day 1 post printing, $n = 5$. d) Immunostaining reveals a neuronal (TUJ1$^+$) signal in printed tissues that increases over time. The lengths of the processes at several time points were quantified ($n > 15$, $p < 0.001$ between all three groups). Neural tissues in (a–d) were printed at a cell density of 2×10^7 mL^{-1} as $7 \times 7 \times 4$ droplet networks. e) Left to right: schematic of a printed $7 \times 7 \times 8$ droplet network; the corresponding bright-field image of a printed tissue constructed from cells at 3.5×10^7 mL^{-1}; high-magnification CAM live-staining; 4′,6-diamidino-2-phenylindole (DAPI) nuclear staining of a section from printed tissue all at day 28 ppd. Arrows mark neural rosettes formed at 28 d ppd. f) Immunostaining for neural markers in rosettes: SOX2, CTIP2, and TUJ1. g) Longer differentiation leads to protuberance formation (arrow) and an increasing density of cortical neurons (CTIP2$^+$). The bar chart shows the number of CTIP2$^+$ cell per unit area of 100 × 100 μm at 28 and 56 d ppd, respectively ($n = 6$, $p < 0.001$). h) Mature neurons (MAP2$^+$ and NeuN$^+$) and astrocytes (GFAP$^+$) also appeared after 56 d ppd. Ki67$^+$ cells indicate pockets of sustained proliferation. The bar chart shows the number of GFAP$^+$ cell per unit area of 200 × 200 μm at day 56 ppd ($n = 6$). Scale bars are 200 μm for the bright-field images in (e) and (g), 50 μm for the right-most images of (g) and (h), and 100 μm elsewhere.

higher connectivity at this stage of differentiation (Figure 3f). To determine whether printed neural tissues could respond to stimulation, we exposed the constructs with 65 d ppd to KCl (60 mM), which evoked rapid Ca^{2+} transients (Figure 3g–i).

Neural cell process outgrowth and cell migration are key features of the development of the central nervous system.[28] In particular, apical NSCs (radial glia) grow long processes and migrate away from the interior of the developing brain to become basal progenitors and outer radial glia. Additionally, neurons born in the interior extend processes and migrate toward the exterior. To test whether printed tissues could recapitulate these cortex developmental events, we designed a printing scheme (**Figure 4**a) comprising interior hNSCs (orange) encased in a cell-free Matrigel exterior compartment (blue), hNSCs (in)-Matrigel (out). The interior neural cells projected processes into the exterior Matrigel during the first a few days of culture in differentiation medium. The length of the processes increased over time, and was followed by cell migration from the hNSC compartment to the Matrigel compartment (Figure 4b,c). Using red-fluorescent-protein-labeled hNSCs (RFP-hNSCs), we further confirmed the process projection and the migration of RFP-hNSCs into the initially cell-free Matrigel compartment (Figure 4c). At day 28 ppd, neurons had filled the Matrigel compartment and immunostaining

© 2020 The Authors. Published by WILEY-VCH Verlag GmbH & Co. KGaA, Weinheim

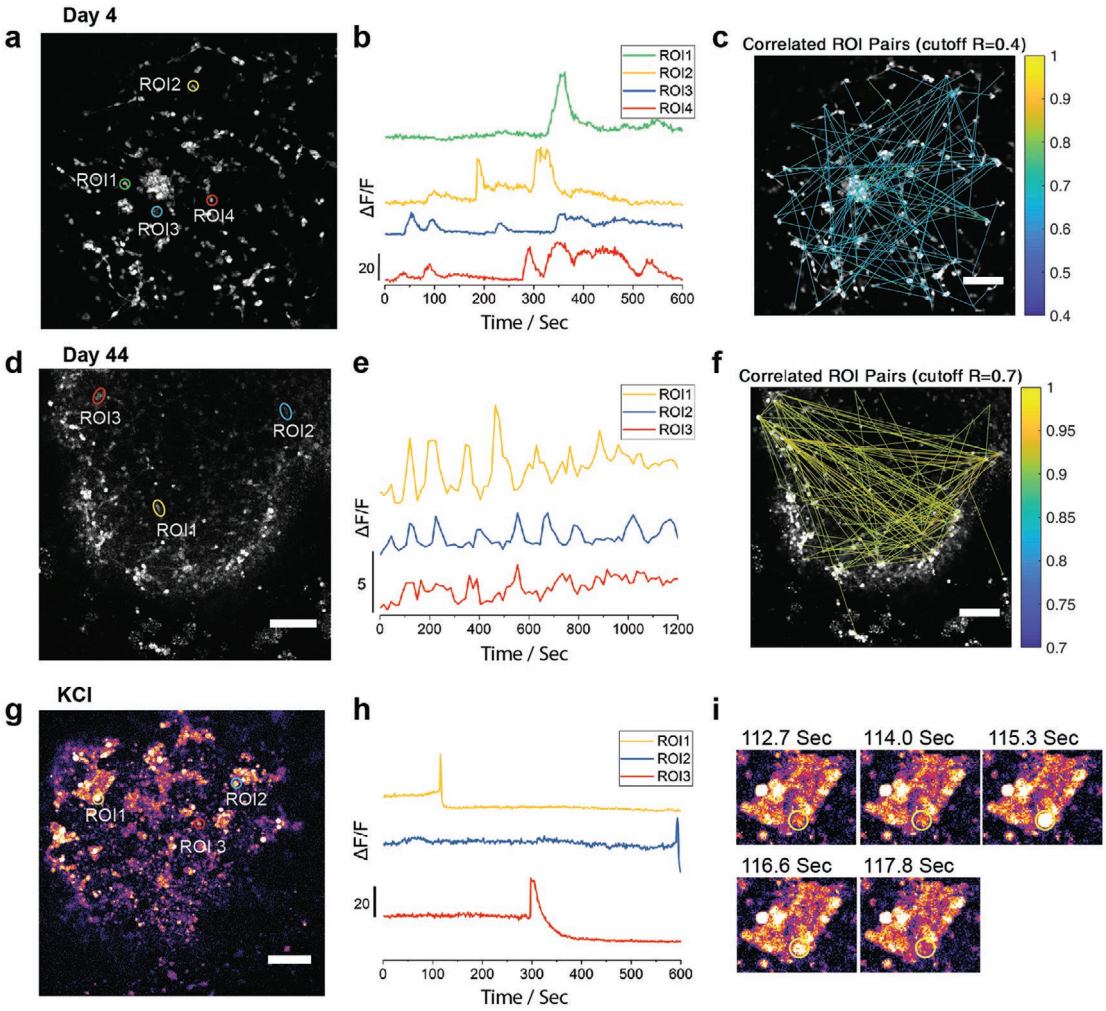
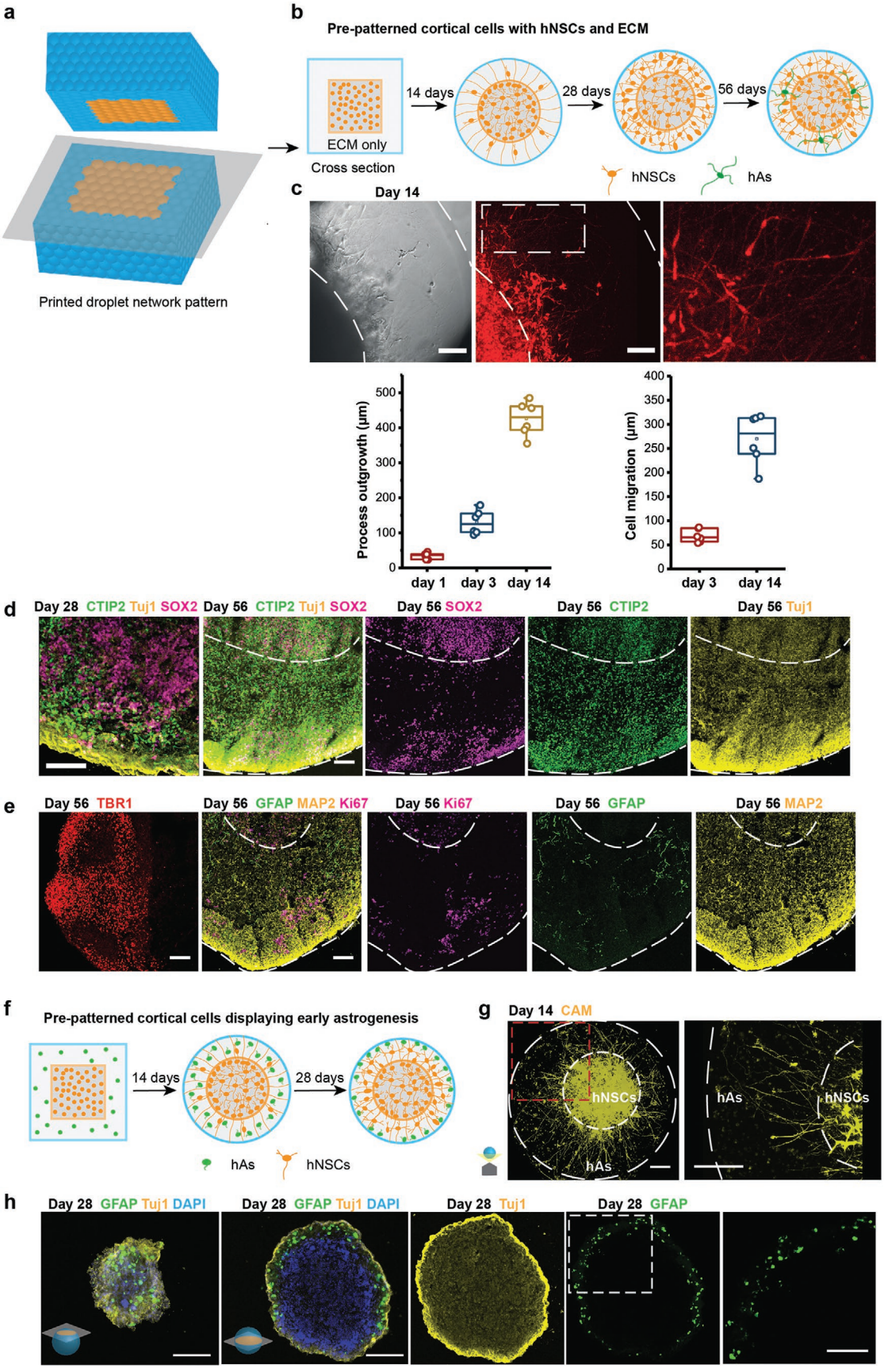


Figure 3. Functional and connected neural networks emerge from printed neural tissues. a) Fluo-4 calcium live imaging of printed neural tissues revealed spontaneous calcium oscillations at 4 d ppd. b) Single-cell traces are shown, color-coded by their locations in regions of interest as indicated in (a). c) Network plots of correlation coefficients reveal limited communication between printed NSCs at 4 d ppd. d–f), Spontaneous calcium oscillations (d), single-cell traces (e), and correlation coefficient analysis (f) of printed neural tissues at 44 d ppd. The data reveal increased neural communication after a longer period of differentiation. g) Fluorescence intensity map obtained from calcium live imaging at 65 d ppd after KCl (60 mM) treatment. Intensities are false-colored according to the "fire" Look Up Table of Fiji. h) Single-cell traces are shown color-coded according to their locations in the ROIs indicated in (g). i) Individual time-point frames of ROI1 (yellow outline) reveal that KCl induced a rapid calcium transient in a cell. Images are false-colored as in (g). Scale bar for all images is 100 µm.

revealed the presence of progenitors ($SOX2^+$), young neurons ($TUJ1^+$), and deep-layer cortical neurons ($CTIP2^+$, Figure 4d). Further, staining for TBR1 revealed the differentiation of subplate neurons at day 56 ppd (Figure 4e). Astrogenesis also occurred at this time in the previously cell-free compartment together with differentiated neurons ($MAP2^+$) and proliferating cells ($Ki67^+$). These data show that the interior printed cells were able to extend processes and migrate into the cell-free exterior, recapitulating aspects of cortical development in a cell autonomous manner.

Since astrocytes regulate axon outgrowth and cell migration in adult neurogenic niches and in pathology, we hypothesized that they may play a role in these events during neurodevelopment. To address this question and test if astrocytes printed together with Matrigel in the exterior compartment affect the above results, we 3D printed primary human cerebral cortex astrocytes around hNSCs. hNSCs and human astrocytes (hAs) were printed in an hNSCs (in)-hAs (out) pattern with a higher density of hNSCs (3.5×10^7 mL^{-1}) than hAs (1.0×10^7 mL^{-1}) to model the early stage of astrogenesis (Figure 4f). Similar to the progression observed with hNSCs (in)-Matrigel (out), interior neural cells projected long processes into the exterior hAs compartment, which was followed by neural cell migration (Figure 4g,h and Figure S5, Supporting Information). The neural cells distributed themselves throughout the network with many moving from the interior to the exterior compartment. Unexpectedly, we did not observe hAs in the interior compartment by day 28 ppd. The hAs not only remained in the exterior compartment but moved to the surface of the constructs (Figure 4h). These results suggest astrocyte positioning may be restricted by the interior compartment, which was primarily neuronal.

© 2020 The Authors. Published by WILEY-VCH Verlag GmbH & Co. KGaA, Weinheim



© 2020 The Authors. Published by WILEY-VCH Verlag GmbH & Co. KGaA, Weinheim

Using confocal microscopy, we reconstructed z-stack images of day 28 ppd hNSCs (in)-Matrigel (out) and hNSCs (in)-hAs (out) printed tissues. Unexpectedly, we observed the formation of neural process bundles in the hNSCs (in)-hAs (out) tissues, but not in the hNSCs (in)-Matrigel (out) tissues (**Figure 5**a,b). This was not due to preferential axonal growth into the hAs-containing domains since the TUJ1$^+$ neuronal processes grew equally well into cell-free Matrigel or astrocyte-containing exterior compartments (Figure 5c). The process bundles formed in the hAs compartment had an average width of 65 ± 22 μm ($n = 7$) compared to 5 ± 3 μm ($n > 7$) in the Matrigel-only compartment (Figure 5d). These data suggest astrocyte-induced neural fasciculation, which was previously observed in mice.[29] To confirm this, we also printed an hAs (left)-hNSCs (right) pattern and found that hNSCs projected processes toward the hAs compartment (Figure 5e). Moreover, progenitors (SOX2$^+$) aligned along the bundled processes indicating axon-guided cell migration (Figure 5e,f). The majority of the migrating cells subtended an angle of $< 20^o$ with an associated process bundle (Figure 5g). Although the starting density of the hAs (1.0×10^7 mL^{-1}) was less than that of the hNSCs (3.5×10^7 mL^{-1}), similar neural cell density was observed in both compartments at day 28 ppd (Figure S6, Supporting Information), suggesting neural cell migration into the astrocyte compartment. Notably, TUJ1$^+$ neuronal processes appeared to be preferentially bundled in the hAs compartment but not in the NSCs compartment (Figure 5f), again suggesting astrocyte-mediated neural fasciculation. Our data show that astrocytes exert a profound effect on the late developmental event of axonal bundling.

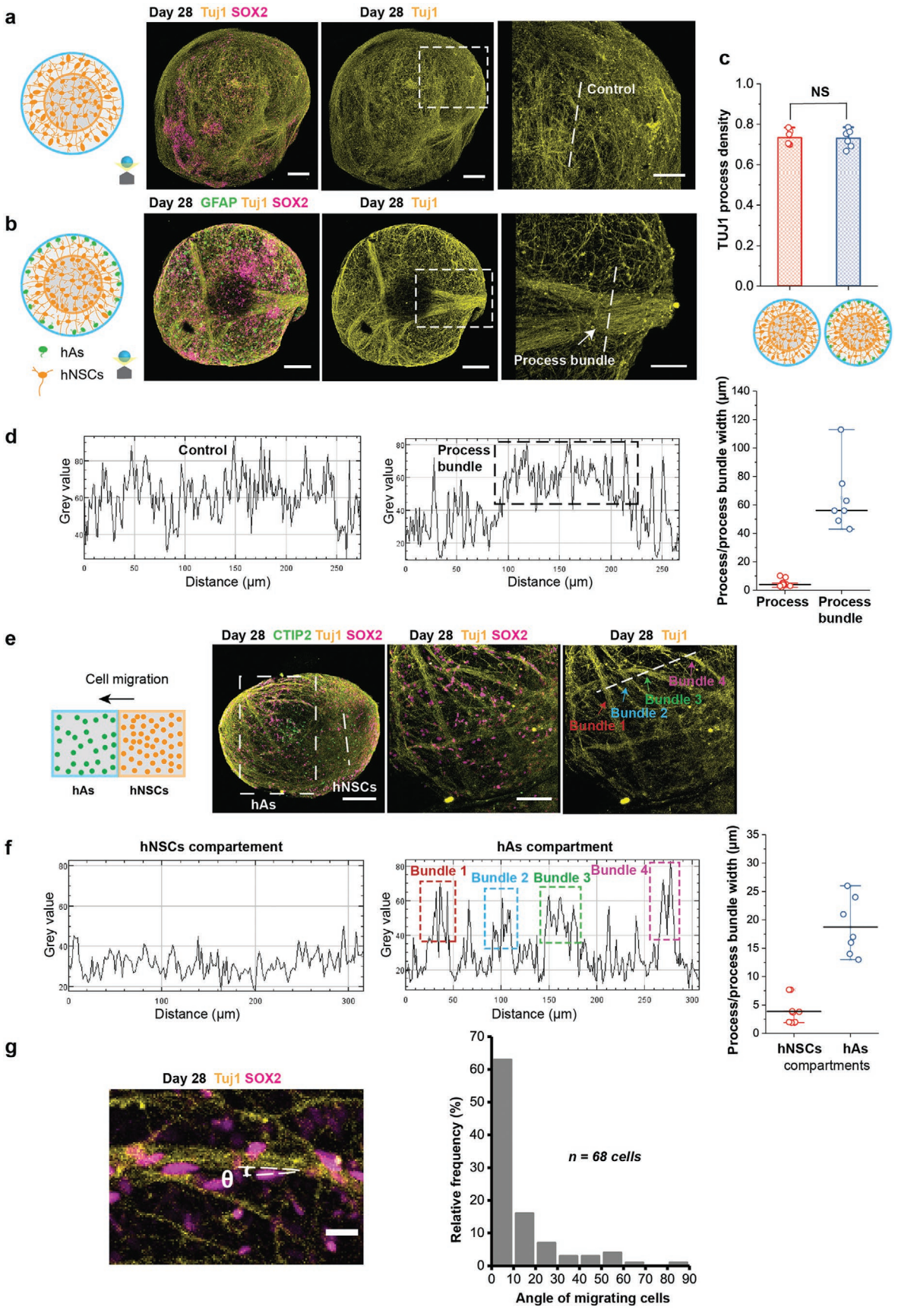
Recent advances in rapid cell programming allow the production of mature neurons and astrocytes in just a few weeks.[21,22,30] These fast programming methods may provide important sources of cells for 3D printing of mature brain tissues quicker than classic reprogramming. We first tested whether we could construct viable differentiated cortical tissues by using rapidly matured human cortical neurons (hCNs) with hAs. Because the hCNs do not proliferate in 2D culture and cannot be harvested without damage after seeding, we added them directly into the bioink after thawing (**Figure 6**a). We first 3D printed homogeneously mixed hCNs and hAs at a density of 1.75×10^7 mL^{-1} for each cell type. After 13 d, printed hCNs had produced long axons (Figure 6b). These mature neurons also expressed MAP2, the glutamatergic neural marker vGlut1, and the synaptic marker SYP (Figure S7, Supporting Information). Both hCNs and hAs retained their homogenous distribution throughout the printed constructs during 13 d in culture.

Studies in mouse models suggest that cortical astrocytes are domain-specific and restricted to their birth place, and cannot migrate even after injury.[31,32] Therefore, to investigate hA migration, we preorganised neurons and astrocytes in spatially segregated compartments, either as hCNs (in)-hAs (out) or the reverse (Figure 6c). In the hCNs (in)-hAs (out) constructs, the hCNs migrated to the astrocyte compartment after less than 2 weeks, whereas hAs mostly remained in the outer compartment with a small fraction, ≈7%, migrating to the center of the constructs (Figure 6c,d). This is similar to and supportive of our data in Figure 4f–h showing neural migration from the interior to the exterior astrocyte-containing compartment, whereas astrocytes remained in the outer compartment. In the hAs (in)-hCNs (out) constructs, ≈80% of the hAs remained in the center of the structure (Figure 6d). Thus, in both prepatterned constructs, hAs maintained their segregation from neurons but not vice versa, showing a nonreciprocal functional interaction.

One of the most powerful tools in developmental biology is heterotopic and heterochronic transplantation of tissues, such as Spemann and Mangold's[33] seminal work that uncovered the neural organizer. Juxtaposition of tissue in artificial patterns allowed the eventual discovery of molecular mechanisms and signaling pathways necessary for development. However, it has been a challenge to juxtapose small clusters of distinct cells to ask more fine-grained questions, until the advent of 3D bio-printing. Astrocytes are well-distributed in different layers of cortex and in close contact with neurons.[34] By pre-positioning astrocytes and cortical neurons with different patterns, we demonstrated that neurons readily migrate into astrocyte domains but that astrocytes prefer to remain segregated from neurons. These observations are consistent with previous reports that astrocytes have limited capacity for migration from their birth locations. However, by experimentally pre-positioning astrocytes separately but next to NSCs, we surprisingly observed that astrocytes assist axonal bundling which is a prelude to tract formation. With the future development of hiPSC-derived region-specific brain cells, different

Figure 4. Prepatterning cell-autonomous process outgrowth and cell migration. a) 3D-printed droplet network used for patterned cortical tissues: a $7 \times 7 \times 7$ droplet network (orange) at the center of a $13 \times 13 \times 13$ droplet network (blue). b) Progression observed for tissues in which hNSCs are encased in Matrigel, as shown in (a) (hNSCs yellow, Matrigel blue). During the first 14 d of differentiation, hNSCs projected processes into the Matrigel compartment. Cell migration followed. Migrated cells filled the Matrigel compartment at 28 d ppd. Astrogenesis occurred at 56 d ppd. Notably, the printed constructs adopted a more spherical geometry after weeks in culture (Figure S3b, Supporting Information). c) Printed fluorescently labeled hNSCs showed cell migration. Top: Live images from RFP-hNSCs showed the projection of processes and cell migration into the Matrigel compartments at 14 d ppd. The dashed lines indicate the boundaries of the inner and outer compartments and the dashed box shows the zoomed-in area of the following image. Bottom: The length of process outgrowth was quantified at 1, 3, and 14 d ppd ($n = 6$ for each time points, $p < 0.005$ between all three groups). The distance of cell migration was quantified at 3 and 14 d ppd ($n = 6$ for each time point, $p < 0.005$). d) Immunostaining reveals that printed tissues contain progenitors (SOX2$^+$), young neurons (TUJ1$^+$), and cortical neurons (CTIP2$^+$) at 28 and 56 d ppd. e) TBR1 staining reveals differentiation into deep-layer cortical neurons at 56 d ppd. Also at this stage, printed constructs contain mature neurons (MAP2$^+$), a small number of astrocytes (GFAP$^+$) and proliferating cells (Ki67$^+$). f) Progression observed for hNSCs encased in hAs, as shown in (a) (hNSCs yellow, hAs blue). hNSCs project processes into the hAs compartment (14 d ppd). Cell migration follows (28 d ppd). hAs remained at the periphery of the tissues. The cell densities during the printing, NSCs (3.5×10^7 mL^{-1}) and hAs (1×10^7 mL^{-1}), mimicked early-stage astrogenesis. g) CAM live-staining image of printed tissues revealed processes that cross from the hNSCs compartment to the hAs compartment. h) Immunostaining reveals the cellular architecture of 3D tissues. The surface contains evenly distributed neurons (TUJ1$^+$) and astrocytes (GFAP$^+$). The section through a central plane shows neurons within a shell of astrocytes. DAPI and TUJ1 staining revealed that hNSCs have migrated toward the astrocyte compartment. Scale bars are 200 μm in (g) (left image), and (h) (first two images) and 100 μm in the rest of the images.

© 2020 The Authors. Published by WILEY-VCH Verlag GmbH & Co. KGaA, Weinheim



© 2020 The Authors. Published by WILEY-VCH Verlag GmbH & Co. KGaA, Weinheim

combinations of precursor and mature cells could be assembled through bioprinting to probe local or distant cross-region brain activities and malfunctions. For example, deep and upper layers of cortical cells might be printed in layered structures to study cell migration across different cortical layers.

To achieve such biological insights, we developed a technique that can be used to print a variety of soft tissues with ECM and without the need to add hard materials. Our technique could potentially be applied to other matrices, such as organ/tissue-derived or artificial ECM, to provide tailored microenvironments in printed 3D tissues. The fabrication of tissue constructs with physiologically relevant cellular microenvironments is crucial for the study of tissues with limited accessibility, such as the human brain. By using Matrigel as the sole printing matrix, we have demonstrated that 3D bioprinting can be applied to the production of cortical tissues without affecting the viability, function and self-organization of the incorporated cells. Bioprinting assigns specific cell types to predetermined initial positions, unlike the process of organoid formation. This spatial prepatterning not only gives better control over self-organization processes, but also allows the generation of unnatural patterns allowing interrogation of the underlying mechanisms of self-organization.

Finally, we demonstrated that by combining our technique with fast neuron programming, differentiated cortical tissues can be constructed within weeks, whereas organoids take months to develop. Although organoids can yield most brain cell types following developmental progression, later-born cells can take months or more to reach significant numbers. Indeed, 2D culture still has an advantage over 3D culture for the mass production of homogeneous cells. However, by taking advantage of advances in the 2D culture of diverse brain cell types, brain tissues from later stages of differentiation might be generated through prepatterned constructs in a fast manner. Together, our data suggest that 3D bioprinting can be applied to spatially position distinct cells to construct 3D tissue models and guide self-organization. The approach can be applied to study human brain developmental processes such as cortical expansion and astrocyte migration/segregation. Finally, diseases could also be modeled by incorporating reprogrammed patient cells with specific genetic mutations.

Experimental Section

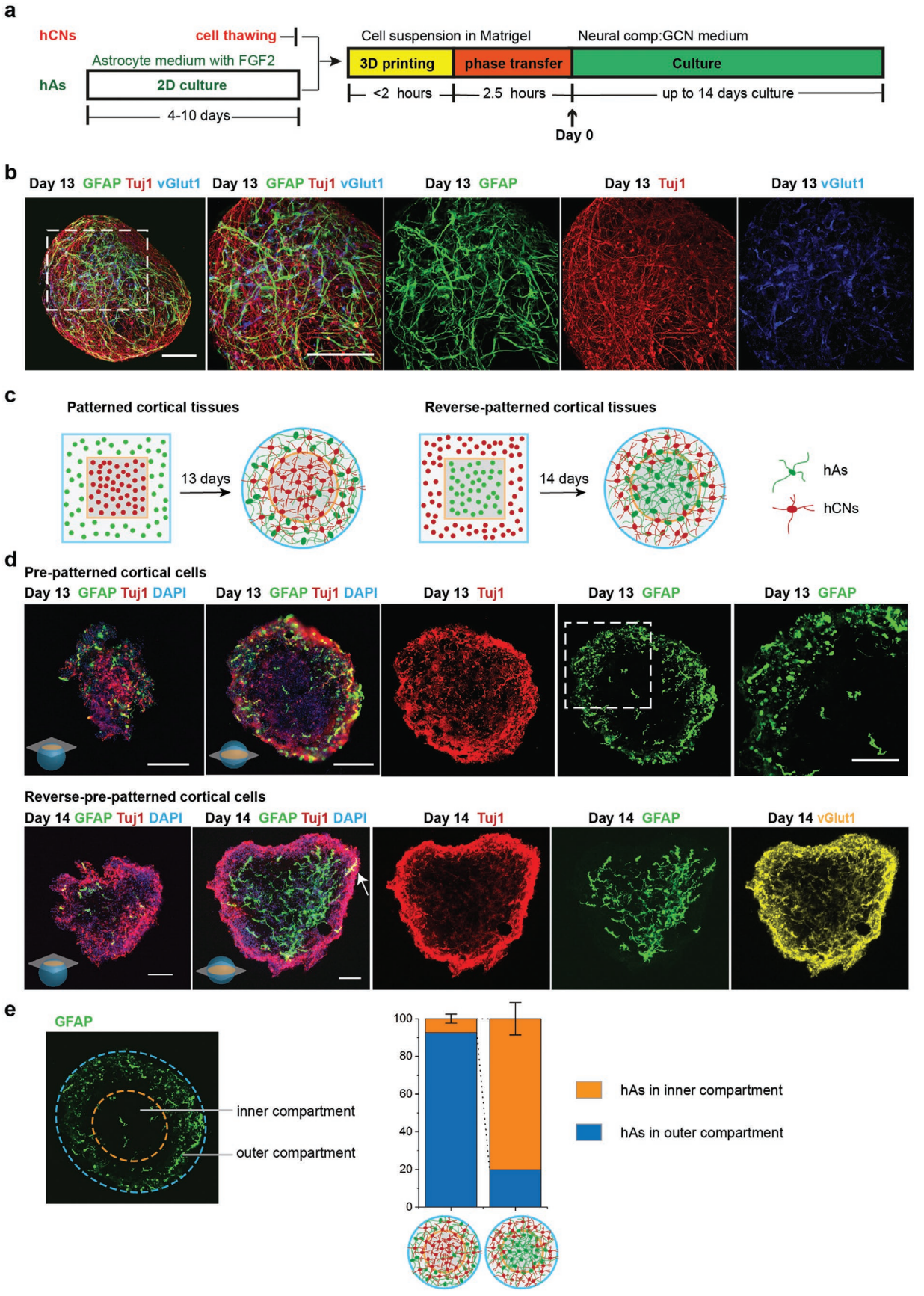
Printer setup: The printer was modified from what was previously described[19] to adapt it to viscous materials and high cell densities (up to 3.5×10^7 mL^{-1}). A more powerful piezo-electric driver with voltage limits of ±130 V was used to produce a higher ejection force (Supporting Information). A Peltier-based temperature-controlled stage was attached to the printer with a temperature range of –15 to 80 °C. For all experiments, Matrigel-based bioink was printed at ≈5 °C. Glass printing nozzles were modified with (3-aminopropyl)trimethoxysilane (Sigma Aldrich, 281778) to provide a hydrophilic coating, which prevented printing oil from entering the nozzle. The printing oil comprised 4 mg mL^{-1} DPhPC (1, 2-diphytanoyl-*sn*-glycero-3-phosphocholine, Avanti, 850356) in a mixture of undecane and silicone oil AR20 (both from Sigma Aldrich; v:v, 1:4).

Cell Culture And Harvest: Two sources of iPSC-derived hNSCs were used: ax0018 from Axol and hNSCs kindly provided by Dr Sally Cowley (James Martin Stem Cell Facility, Oxford). The ax0018 cells were derived from human fibroblasts (healthy donor) and expressed typical markers of cerebral cortical neural stem and progenitor cells, such as PAX6, FOXG1, and nestin (manufacturer's data). The cells were cultured according to the manufacturer's instructions. Briefly, the cells were thawed and seeded on 2% Matrigel (Corning, 354230)-coated 6-well plates in Neural Plating-XF medium (Axol, ax0033), followed by expansion on the second day with Neural Expansion-XF medium (Axol, ax0030), containing EGF (20 ng mL^{-1}, Axol, ax0047X) and FGF2 (20 ng mL^{-1}, Axol, ax0047). Cells were harvested at ≈80% confluency (ranging from 4 to 7 d postplating) for bioink preparation. The NSCs provided by Dr Cowley were human fibroblasts reprogrammed according to the protocol of Shi et al.[2] The resulting cortical NSCs were grown as 2D adherent cultures on Matrigel-coated 6-well plates in NMM: 1:1 v/v N-2 medium and B-27 medium. N-2 medium contains advanced DMEM/F12 (Gibco, 12634-010), 1 × N-2 (Gibco, 17502048), 5 μg mL^{-1} insulin (Sigma, I9278), 100 μM 2-mercaptoethanol (Gibco, 31350-010), 1 mM GlutaMax (Gibco, 35050-038), 100 μM nonessential amino acids (NEAA) (Gibco, 1605380), and 50 U mL^{-1} penicillin and streptomycin (Gibco, 15140-122). B-27 medium contains neurobasal medium (Gibco, 21103-049S), 1 × B-27 (Gibco, 17504044), 1 mM GlutaMax (Gibco, 35050-038), and 50 U mL^{-1} penicillin and streptomycin (Gibco, 15140-122). Cultured hiPSC-NSCs were harvested between day 30 and 45 of the differentiation protocol. Cells were incubated in accutase solution (Sigma Aldrich) for 5 min at 37 °C and dissociated to a single cell solution by gentle pipetting. We did not observe obvious differences after printing between the two iPSC-NSC lines.

RFP-hNSCs derived from RFP-iPSCs were also provided by Dr Sally Cowley.[35] The cells were cultured and passaged the same as the nonlabelled hNSCs from Dr Sally Cowley except for the addition of 2.5 μg mL^{-1} puromycin in NMM for RFP selection.

Figure 5. Astrocytes induce axonal fasciculation in prepatterned cortical tissues. a) Left: 2D cross-section showing the prepatterned hNSCs (in)-Matrigel (out) constructs at 28 d ppd. Right: confocal z-projection images reveal that both progenitors (SOX2$^+$) and young neurons (TUJ1$^+$) are on the surface of the structures at 28 d ppd. The dashed box shows the zoomed-in area in the following image, in which the dashed line indicates the site of the fluorescence profile in (d) (control). b) Left: 2D cross-section showing the prepatterned hNSCs (in)-hAs (out) construct at 28 d ppd. Right: confocal z-projection images reveal the existence of astrocytes (GFAP$^+$), neurons (TUJ1$^+$), and neural progenitors (SOX2$^+$) on the tissue surface. The dashed box indicates the zoomed-in area shown in the following image. Importantly, process bundles were observed in (b) but not in (a), indicating astrocyte-assisted neural fasciculation. The dashed line indicates the site of the fluorescence profile in (d) (through the process bundle). c) Process densities are similar for both constructs (a and b). Process density is calculated as the ratio of the TUJ1$^+$-fluorescence area to the total area ($n = 6$, $p > 0.9$, NS: not significant). d) Profile plots of fluorescence intensity along the white dashed lines indicated in (a) and (b). The black dashed box shows the position of a neural process bundle. Whisker plot indicates the width of bundles in printed cortical tissues (b) compared to (a) (control, $n \geq 7$, $p < 0.001$). Each point indicates the width of one bundle (in (b)) or a process (in (a)). e) Left: Cross-section of the design, hAs (left)-hNSCs (right). Right: confocal z-projection images reveal neural progenitors (SOX2$^+$) migrating along neural process bundles. The dashed box shows the zoomed-in area for the following images. The dashed lines indicate the sites for the fluorescence profile in (f) (Left, hNSCs compartment and right, process bundles 1–4 in hAs compartment). f) Left: fluorescence profiles show that process bundles exist in the hAs compartment but not in the hNSCs compartment. Right: Whisker plot comparing the width of process bundles in the hAs compartment with the process at the hNSCs compartment in (e) ($n \geq 7$, $p < 0.001$). g) Alignment of migrating cells with process bundles. Left: example of a measurement of the angle between a migrating cell and a process bundle. Right: bar chart shows that a majority of cells subtend an angle of < 20° with an associated process bundle ($n = 68$ cells). Scale bars are 200 μm in (a) (first two images), (b) (first two images), and (e) (first image), 20 μm in (g), and 100 μm in the rest of the images.

© 2020 The Authors. Published by WILEY-VCH Verlag GmbH & Co. KGaA, Weinheim



© 2020 The Authors. Published by WILEY-VCH Verlag GmbH & Co. KGaA, Weinheim

iPSC-derived hCNs were purchased from Bit Bio and thawed according to the manufacturer's instructions. The cells were used directly for bioink after thawing, without prior 2D cell culture.

Human primary astrocytes (hAs, ScienCell, catalogue #1800) were cultured according to the manufacturer's instructions. Briefly the cells were thawed and cultured on poly-L-lysine (Sigma, P4707) coated flasks in astrocyte medium containing: DMEM/F12 (Gibco, 11320033), 1 × N-2 (Gibco, 17502048), 1 × B-27 (Gibco, 17504044), 100 µM NEAA (Gibco, 1605380), 100 µM 2-mercaptoethanol (Gibco, 31350-010), 10 ng mL^{-1} FGF2 (Gibco, 13256029), 10% FBS (Gibco, 10270-106), and 1 mM GlutaMax (Gibco, 35050-038). Half of the culture medium was exchanged with fresh medium every second day. Cells were harvested by incubation with 1 × trypsin-EDTA solution (0.5 g L^{-1} trypsin, Sigma Aldrich, T3924) for 3 min according to the manufacturer's instructions.

Bioink Preparation and Printing Procedure: Prior to use, total cell number and cell viability were determined by trypan blue staining by using a Countess II automated cell counter (ThermoFisher). Matrigel was used without dilution and thawed at 4 °C before use. Cells were dissociated to form suspensions of individual cells. After centrifugation (5 min at 200 × *g*), the supernatant was removed. A volume of thawed Matrigel, calculated based on the required cell-density of the bioink, was then added to the pellet and the cells were suspended on ice to generate the bioink, which was loaded into printer nozzles and kept at ≈4 °C during the printing process. Printing was performed by using maps entered into the custom control software as previously described.[19] The printing process took 1–2 h to generate multiple droplet networks.

Phase Transfer of Printed Network: Printed networks were incubated at RT for 30 min before transfer to a tissue culture incubator at 37 °C for 2 h. Half of the oil was then removed and replaced with silicone oil. This oil exchange process was repeated five times to dilute lipid. Culture medium was then added to replace half of the oil. The medium was then exchanged a further four times (half of the medium was exchanged each time) to remove any residual oil.

The phase-transferred tissue constructs with hNSCs (with and without astrocytes) were then cultured in NMM to support differentiation. Two-thirds of the medium were exchanged with fresh medium every 2–3 d.

Printed tissues with hCNs (with and without astrocytes) were cultured in comp:GCN medium with 10 µM ROCK inhibitor (Stratech Scientific, S1049-SEL) and 1 µg mL^{-1} doxycycline (Sigma Aldrich, D9891) for the first 2 d and doxycycline only for another 2 d. Comp:GCN medium alone was then used for up to 10 d. Half of the medium was exchanged with fresh medium every second day. The comp:GCN medium contains neurobasal medium (Gibco, 21103-049S), 1 mM GlutaMax (Gibco, 35050-038), 25 µM 2-mercaptoethanol (Gibco, 31350-010), 1 × B-27 (Gibco, 17504044), 10 ng mL^{-1} NT3 (R&D Systems, 267-N3-025), and 5 ng mL^{-1} BDNF (R&D Systems, 248-BD-005).

Cell Staining and Viability Calculation: Printed tissues were incubated with 2.5 µM calcein-AM (Cambridge Biosciences Ltd) and 5.0 µM propidium iodide (Sigma Aldrich) for 30 min before imaging. Four randomly selected fields of each printed network at different z-heights were imaged with ≈30× magnification by using fluorescence confocal microscopy (Leica SP5). Dead cells were counted manually due to their low number. Live cells were counted using Fiji[36] by setting a threshold that matches the Calcein AM (CAM) fluorescence of the live cells, followed by particle analysis (size setting: 2 micron^2-Infinity). The cell number of clusters of cells was determined by using the area of a cluster divided by the area of an average cell. The live/dead cell numbers from the four images of one sample were averaged to give each data point and five samples were used to determine the viability as shown in Figure 2c ($n = 5$).

Tissue Sectioning, Immunostaining, and Imaging: Printed tissues were fixed in 4% v/v paraformaldehyde (Sigma Aldrich) for 30 min at RT and then quenched in 50 mM glycine (Sigma Aldrich). Tissue sectioning was performed using a cryostat to generate 30-µm-thick sections for immunohistological analysis. Samples were incubated at 37 °C for 15 min, washed in phosphate buffered saline (PBS) and then blocked for 1 h at RT with 5% v/v goat serum (Sigma Aldrich) in triton phosphate buffered saline (TPBS) containing 0.1% v/v Triton X-100 (Fisher Scientific). Primary antibodies (Table 1, Supporting Information) were added in blocking solution and samples were incubated for 2 h at 37 °C. Subsequently, samples were washed in PBS then incubated with secondary antibodies for 2 h at 37 °C. Samples were then washed in PBS, incubated with 4′,6-diamidino-2-phenylindole (1/1000 dilution) in TPBS for 15 min and washed again. All printed networks were imaged using fluorescence confocal microscope (Leica SP5) and wide-field light microscope (Leica DMI 8).

Process Length Analysis: TUJ1 immunostaining was performed on printed tissues as described above. Imaging was conducted with a confocal microscope using a 20× objective and z-projection images were used for quantification. The length of the $TUJ1^+$ processes emanating from the cell bodies at 4, 8, and 14 d ppd was quantified by using the Fiji "freehand line" tool and the values are summarized in Figure 2d ($n > 15$, $p < 0.001$ between all groups).

Cell Number Analysis of $CTIP2^+$ and $GFAP^+$ cells: Printed tissues were fixed and cut into 30 µm sections before immunostaining. $CTIP2^+$ cells were counted as cell number per unit area in a 100 × 100 µm field at 28 and 56 d ppd ($n = 6$, $p < 0.001$). $GFAP^+$ cells were counted as cell number per unit area in a 200 × 200 µm field at day 56 ppd ($n = 6$).

Calcium Imaging and Correlation Analysis: A Fluo-4 Direct calcium assay kit (Invitrogen, F10471) was used according to the manufacturer's instructions to measure calcium activities. Briefly, printed neural tissues were transferred to 48-well plates and incubated with NMM/Fluo-4 calcium imaging reagents (v:v, 1:1) for 1 h at 37 °C. Both spontaneous and evoked calcium recordings were recorded at 37 °C by fluorescence confocal microscopy (Leica SP5) at 1 frame per 2 s for Fig. 3a, 1 frame per 15 s for Fig. 3d, and 1 frame per 1 s for Fig. 3g. Preprocessing and analysis of time-lapse calcium recordings were performed in MATLAB. The nonrigid image registration algorithm scale-invariant feature transform (SIFT) Flow was used to correct for local deformations of printed tissue relative to the initial frame. Individual neuronal somata were manually selected as ROIs, and the pixel mask in the local area was refined using independent component analysis (ICA)-based demixing of fluorescent transients. $\Delta F/F_0$ at time t was calculated with a moving baseline as

$$\frac{F(t)}{\min\left(\overline{F(x)}_{(t-\tau_2)<x<t)}\right)} \quad (1)$$

Figure 6. Fast production of differentiated cortical tissues. a) Timeline for the production of 3D differentiated cortical tissues. iPSC-derived human cortical neurons (hCNs) were used for bioink without preculture, whereas hAs were harvested from 2D culture at day 4–10. Further details are described in the Experimental section. b) Immunostaining of tissues constructed from mixed hCNs ($TUJ1^+$ and $vGlut1^+$) and hAs ($GFAP^+$) at day 13 post printing. c) Schematic of patterned and reverse-patterned cortical tissues and the observed progression in culture. d) Top: immunostaining of tissue sections (surface and a central plane) at 13 d ppd indicates a thicker astrocyte shell compared to the astrocyte shell of the tissue in Figure 4h (same pattern but with hNSCs). hCNs have invaded the astrocyte compartment, while most hAs have remained in the outer compartment with a small fraction of hAs having migrated toward the center. Bottom: immunostaining of tissue sections (surface and a central plane) from the reverse-patterned cortical tissue at 14 d ppd. The arrow indicates an astrocyte that has migrated into the exterior neuron compartment. Synaptic staining (vGlut1) confirmed the mature differentiated stage of the hCNs. e) Left: example of segmentation used to define the inner (blue) and outer (orange) compartments that are used for the stacked bar chart (right). The two compartments have equal areas. Right: Stacked bar chart of hAs distribution for the two different patterns. Tissues were constructed with hCNs (red, 3.5×10^7 mL^{-1}) and hAs (green, 3.5×10^7 mL^{-1}). Scale bars are 200 µm in (b) (first image) and (d) (first two images of each row) and 100 µm in the rest of the images.

© 2020 The Authors. Published by WILEY-VCH Verlag GmbH & Co. KGaA, Weinheim

where:

$$F = F_{raw} - F_{neuropil} \quad (2)$$

$$\overline{F(x)} = \frac{1}{\tau_1}\int_{x-\tau_1/2}^{x+\tau_1/2} F(\tau)\,d\tau \quad (3)$$

$$\tau_2 = 75\text{s (5 frames)} \quad (4)$$

$$\tau_1 = 45\text{ s (3 frames)} \quad (5)$$

To determine the active frames of a neuron, an eight-frame moving standard deviation ($\sigma_{mov)}$) was calculated along the time series, with the 10th percentile σ_{mov} taken as the deviation of baseline noise. Active frames were defined as $3\cdot\sigma_{mov}$ above the mean intensity value. Cross-correlation at zero time-lag is calculated for all pairs of neurons. Confidence intervals (CI) of 99.9% for the correlation coefficients were determined via cross-correlation of 1000 shuffled $\Delta F/F_0$ traces of each neuron pair, where each shuffle maintains sequential blocks of active frames ($3\cdot\sigma_{mov}$) to preserve any slow transients in a calcium signal. Only pairs with coefficients > 99.9% CI were considered for further analysis.

Process Outgrowth and Cell Migration Analysis: Printed tissues with RFP-hNSCs encased in Matrigel were monitored by live imaging. Both process projection and cell migration from the RFP-hNSC compartment into the Matrigel compartment were analyzed using the Fiji "freehand tool." The length of process outgrowth was quantified at 1, 3, and 14 d ppd ($n = 6$ for each time point $p < 0.005$ between all three groups). The distance of cell migration into the cell-free Matrigel was quantified at 3 and 14 d ppd ($n = 6$ for each time point $p < 0.005$). The box charts in Figure 4c show mean, interquartile range (box), and 5th and 95th percentiles (whiskers).

Process Density, Process Bundle Width, and Cell Alignment Analysis: Printed tissues were fixed and immunostained at 28 d ppd. Process densities were calculated as the ratios of the TUJ1$^+$-fluorescence area to the total area ($n = 6$, $p > 0.9$, not significant). The fluorescence intensities of process bundles were plotted with Fiji "profile plots" and the widths of the bundles were analyzed in Figure 5d,f ($n \geq 7$, $p < 0.001$, for both plots). The alignment of migrating cells was quantified as the angle between the cells and associated process bundles by using the Fiji "angle tool" ($n = 68$ cells). The percentages of cells with specific ranges of angles (0°–10°, 10°–20°, ... , 80°–90°) were calculated and presented as relative frequency in Figure 5g.

hAs Segregation Analysis: Printed tissues with either hCNs (in)-hAs (out) or hAs (in)-hCNs (out) patterns were sectioned, and sections from a central plane of the tissues were immunostained with antibodies for TUJ1, SOX2, and GFAP as described above. The inner and outer compartments (of equal areas) were defined as shown in Figure 6e. Fluorescent areas (GFAP$^+$) in both inner and outer compartments were quantified using Fiji to generate the stacked bar chat. $n = 3$ for both patterns.

Statistics: Data are presented either as mean ± standard deviation (Figures 2c,d and 6c) or mean with 5th and 95th percentiles and/or interquartile range (Figures 2g,h, 4c, and 5c,d,f). Statistical analyses were performed using GraphPad Prism 8 or Origin. Statistical analysis was performed using the *t*-test for two groups or one-way analysis of variance (ANOVA) with Tukey's multiple comparisons test when more than two groups were compared.

Supporting Information

Supporting Information is available from the Wiley Online Library or from the author.

Acknowledgements

The authors are grateful to Dr Katerina Aravantinou-Fatorou and Dr Dimitra Thomaidou (Hellenic Pasteur Institute, Greece) for their help in human astrocyte culture. The authors thank Rosemary Clare Burke for her help with drawing 3D schemes. The authors are grateful to Dr Sally Cowley (James Martin Stem Cell Facility, Oxford) for providing hNSCs and RFP-hNSCs. The authors thank Yongcheng Jin (Department of Chemistry, University of Oxford) for culturing RFP-hNSCs, and Timothy Powell and Kevin Valentine (Electronic workshop, Department of Chemistry, University of Oxford) for making the electronic components for the printer. The authors also thank Howard Lambourne and Les Hill (Mechanical workshop, Department of Chemistry, University of Oxford) for making mechanical components for the printer. This research was supported by a European Research Council Advanced Grant and OxSyBio. FS was funded by the University of Oxford John Fell Fund 152/055. L.Z., F.S., and H.B. conceived the project and experimental design and wrote the manuscript. L.Z. performed experiments and analyzed data. A.W. assisted with neural cell culture, printing experiments, and proofreading of the manuscript. Y.L. conducted 2D culture experiments with the hNSCs from Dr Cowley's laboratory. D.C. and H.K. performed calcium imaging correlation analysis.

Conflict of Interest

H.B. is the Founder of, a Director of, a share-holder of, and a consultant for OxSyBio, a company engaged in the development of printed tissues and tissue-like materials.

Keywords

3D bioprinting, droplets, lipid bilayers, neural tissue, neural differentiation

Received: March 30, 2020
Revised: May 1, 2020
Published online:

[1] C. M. Nelson, M. J. Bissell, *Annu. Rev. Cell. Dev. Biol.* **2006**, *22*, 287.
[2] Y. C. Shi, P. Kirwan, J. Smith, H. P. C. Robinson, F. J. Livesey, *Nat. Neurosci.* **2012**, *15*, 477.
[3] M. A. Lancaster, M. Renner, C. A. Martin, D. Wenzel, L. S. Bicknell, M. E. Hurles, T. Homfray, J. M. Penninger, A. P. Jackson, *Nature* **2013**, *501*, 373.
[4] N. D. Amin, S. P. Pasca, *Neuron* **2018**, *100*, 389.
[5] A. Warmflash, B. Sorre, F. Etoc, E. D. Siggia, A. H. Brivanlou, *Nat. Methods* **2014**, *11*, 847.
[6] G. T. Knight, B. F. Lundin, N. Iyer, L. M. T. Ashton, W. A. Sethares, R. M. Willett, R. S. Ashton, *eLife* **2018**, *7*, e37549
[7] F. Birey, J. Andersen, C. D. Makinson, S. Islam, W. Wei, N. Huber, H. C. Fan, K. R. C. Metzler, G. Panagiotakos, N. Thom, N. A. O'Rourke, L. M. Steinmetz, J. A. Bernstein, J. Hallmayer, J. R. Huguenard, S. P. Pasca, *Nature* **2017**, *545*, 54.
[8] G. Y. Cederquist, J. J. Asciolla, J. Tchieu, R. M. Walsh, D. Cornacchia, M. D. Resh, L. Studer, *Nat. Biotechnol.* **2019**, *37*, 436.
[9] H. W. Kang, S. J. Lee, I. K. Ko, C. Kengla, J. J. Yoo, A. Atala, *Nat. Biotechnol.* **2016**, *34*, 312.
[10] T. J. Hinton, Q. Jallerat, R. N. Palchesko, J. H. Park, M. S. Grodzicki, H. J. Shue, M. H. Ramadan, A. R. Hudson, A. W. Feinberg, *Sci. Adv.* **2015**, *1*, e1500758.
[11] M. T. Poldervaart, H. Gremmels, K. van Deventer, J. O. Fledderus, F. C. Oner, M. C. Verhaar, W. J. Dhert, J. Alblas, *J. Controlled Release* **2014**, *184*, 58.

© 2020 The Authors. Published by WILEY-VCH Verlag GmbH & Co. KGaA, Weinheim

[12] B. A. Nerger, P.-T. Brun, C. M. Nelson, *Soft Matter* **2019**, *15*, 5278.
[13] Q. Gu, E. Tomaskovic-Crook, R. Lozano, Y. Chen, R. M. Kapsa, Q. Zhou, G. G. Wallace, J. M. Crook, *Adv. Healthcare Mater.* **2016**, *5*, 1428.
[14] Q. Gu, E. Tomaskovic-Crook, G. G. Wallace, J. M. Crook, *Adv. Healthcare Mater.* **2017**, *6*, 1700175.
[15] R. Lozano, L. Stevens, B. C. Thompson, K. J. Gilmore, R. Gorkin, 3rd, E. M. Stewart, *Biomaterials* **2015**, *67*, 264.
[16] R. Sharma, I. P. M. Smits, L. De La Vega, C. Lee, S. M. Willerth, *Front. Bioeng. Biotechnol.* **2020**, *8*, 57.
[17] D. Joung, V. Truong, C. C. Neitzke, S. Z. Guo, P. J. Walsh, J. R. Monat, F. B. Meng, S. H. Park, J. R. Dutton, A. M. Parr, M. C. McAlpine, *Adv. Funct. Mater.* **2018**, *28*, 1801850.
[18] F. Y. Hsieh, H. H. Lin, S. H. Hsu, *Biomaterials* **2015**, *71*, 48.
[19] G. Villar, A. D. Graham, *Science* **2013**, *340*, 48.
[20] A. D. Graham, S. N. Olof, M. J. Burke, J. P. K. Armstrong, E. A. Mikhailova, J. G. Nicholson, S. J. Box, F. G. Szele, A. W. Perriman, H. Bayley, *Sci. Rep.* **2017**, *7*, 7004
[21] M. Pawlowski, D. Ortmann, A. Bertero, J. M. Tavares, R. A. Pedersen, L. Vallier, M. R. N. Kotter, *Stem Cell Rep.* **2017**, *8*, 803.
[22] Y. S. Zhang, C. Pak, Y. Han, H. Ahlenius, Z. J. Zhang, S. Chanda, S. Marro, C. Patzke, C. Acuna, J. Covy, W. Xu, N. Yang, T. Danko, L. Chen, M. Wernig, T. C. Sudhof, *Neuron* **2013**, *78*, 785.
[23] S. V. Murphy, A. Atala, *Nat. Biotechnol.* **2014**, *32*, 773.
[24] H. Bayley, B. Cronin, A. Heron, M. A. Holden, W. L. Hwang, R. Syeda, J. Thompson, M. Wallace, *Mol. BioSyst.* **2008**, *4*, 1191.
[25] A. B. Toth, A. K. Shum, M. Prakriya, *Cell Calcium* **2016**, *59*, 124.
[26] M. Brini, T. Cali, D. Ottolini, E. Carafoli, *Cell. Mol. Life Sci.* **2014**, *71*, 2787.
[27] Y. Penn, M. Segal, E. Moses, *Proc. Natl. Acad. Sci. USA* **2016**, *113*, 3341.
[28] R. Ayala, T. Z. Shu, L. H. Tsai, *Cell* **2007**, *128*, 29.
[29] S. Minocha, D. Valloton, A. R. Ypsilanti, H. Fiumelli, E. A. Allen, Y. Yanagawa, O. Marin, A. Chedotal, J. P. Hornung, C. Lebrand, *Nat. Commun.* **2015**, *6*, 6887.
[30] I. Canals, A. Ginisty, E. Quist, R. Timmerman, J. Fritze, G. Miskinyte, E. Monni, M. G. Hansen, I. Hidalgo, D. Bryder, J. Bengzon, H. Ahlenius, *Nat. Methods* **2018**, *15*, 693.
[31] H. H. Tsai, H. L. Li, L. C. Fuentealba, A. V. Molofsky, R. Taveira-Marques, H. L. Zhuang, A. Tenney, A. T. Murnen, S. P. J. Fancy, F. Merkle, N. Kessaris, A. Alvarez-Buylla, W. D. Richardson, *Science* **2012**, *337*, 358.
[32] S. Magavi, D. Friedmann, G. Banks, A. Stolfi, C. Lois, *J. Neurosci.* **2012**, *32*, 4762.
[33] H. Spemann, H. Mangold, *Int. J. Dev. Biol.* **2001**, *45*, 13.
[34] N. A. Oberheim, T. Takano, X. Han, W. He, J. H. C. Lin, F. Wang, Q. Xu, J. D. Wyatt, W. Pilcher, J. G. Ojemann, B. R. Ransom, S. A. Goldman, M. Nedergaard, *J. Neurosci.* **2009**, *29*, 3276.
[35] W. Haenseler, S. N. Sansom, J. Buchrieser, S. E. Newey, C. S. Moore, F. J. Nicholls, S. Chintawar, C. Schnell, J. P. Antel, N. D. Allen, M. Z. Cader, R. Wade-Martins, W. S. James, S. A. Cowley, *Stem Cell Rep.* **2017**, *8*, 1727.
[36] J. Schindelin, I. Arganda-Carreras, E. Frise, V. Kaynig, M. Longair, T. Pietzsch, S. Preibisch, C. Rueden, S. Saalfeld, B. Schmid, J. Y. Tinevez, D. J. White, V. Hartenstein, K. Eliceiri, P. Tomancak, A. Cardona, *Nat. Methods* **2012**, *9*, 676.

© 2020 The Authors. Published by WILEY-VCH Verlag GmbH & Co. KGaA, Weinheim